Satellite-Derived Latent Heating Distribution and Environmental Influences in Hurricane Opal (1995)

EDWARD B. RODGERS

Laboratory of Atmospheres, NASA/Goddard Space Flight Center, Greenbelt, Maryland

WILLIAM S. OLSON

Caelum Research Corporation, Silver Spring, Maryland

V. MOHAN KARYAMPUDI AND HAROLD F. PIERCE

Science Systems and Applications Inc., Lanham, Maryland

(Manuscript received 12 September 1996, in final form 7 May 1997)

ABSTRACT

The total (i.e., convective and stratiform) latent heat release (LHR) cycle in the eyewall region of Hurricane Opal (October 1995) has been estimated using observations from the *F-10*, *F-11*, and *F-13* Defense Meteorological Satellite Program Special Sensor Microwave/Imagers (SSM/Is). This LHR cycle occurred during the hurricane's rapid intensification and decay stages (3–5 October 1995). The satellite observations revealed that there were at least two major episodes in which a period of elevated total LHR (i.e., convective burst) occurred in the eyewall region. During these convective bursts, Opal's minimum pressure decreased by 50 mb and the LHR generated by convective processes increased, as greater amounts of latent heating occurred at middle and upper levels. It is hypothesized that the abundant release of latent heat in Opal's middle- and upper-tropospheric region during these convective burst episodes allowed Opal's eyewall to become more buoyant, enhanced the generation of kinetic energy and, thereby, rapidly intensified the system. The observations also suggest that Opal's intensity became more responsive to the convective burst episodes (i.e., shorter time lag between LHR and intensity and greater maximum wind increase) as Opal became more intense.

Analyses of SSM/I-retrieved parameters, sea surface temperature observations, and the European Centre for Medium-Range Weather Forecasts (ECMWF) data reveal that the convective rainband (CRB) cycles and sea surface and tropopause temperatures, in addition to large-scale environmental forcing, had a profound influence on Opal's episodes of convective burst and its subsequent intensity. High sea surface (29.7°C) and low tropopause (192 K) temperatures apparently created a greater potential for Opal's maximum intensity. Strong horizontal moisture flux convergence within Opal's outer-core regions (i.e., outside 333-km radius from the center) appeared to help initiate and maintain Opal's CRBs. These CRBs, in turn, propagated inward to help generate and dissipate the eyewall convective bursts. The first CRB that propagated into Opal's eyewall region appeared to initiate the first eyewall convective burst. The second CRB propagated to within 111 km of Opal's center and appeared to dissipate the first CRB, subjecting it to subsidence and the loss of water vapor flux. The ECMWF upper-tropospheric height and wind analyses suggest that Opal interacted with a diffluent trough that initated an outflow channel, and generated high values of upper-tropospheric eddy relative angular momentum flux convergence. The gradient wind adjustment processes associated with Opal's outflow channel, in turn, may have helped to initiate and maintain the eyewall convective bursts. The ECMWF analyses also suggest that a dry air intrusion within the southwestern quadrant of Opal's outer-core region, together with strong vertical wind shear, subsequently terminated Opal's CRB cycle and caused Opal to weaken prior to landfall.

1. Introduction

It was demonstrated by Rodgers and Pierce (1995) that the evolution of Typhoon Bobbie's large-scale convective rainband (CRB) cycles (Willoughby et al. 1982; Willoughby 1988, 1990) during its mature and decaying stages could be resolved with the aid of both the *F-10* and *F-11* Defense Meteorological Satellite Program (DMSP) Special Sensor Microwave/Imager (SSM/I) data. The study suggested that the increased precipitation in the inertially stable inner core [i.e., within 111 km of the tropical cyclone center (Weatherford 1987)] preceded Typhoon Bobbie's period of intensification. In addition, Bobbie's CRB cycle appeared to be initiated by lower-tropospheric horizontal moisture flux convergence over oceanic regions where sea surface temperatures (SSTs) were greater than 26°C, tropospheric con-

Corresponding author address: Dr. Edward B. Rodgers, Mesoscale Atmospheric Processes Branch (Code 912), Laboratory for Atmospheres, NASA/Goddard Space Flight Center, Greenbelt, MD 20771.

ditions were uniformly moist, and the vertical wind shear was less than 10 m s^{-1}, in agreement with studies by Molinari and Skubis (1985) and Lee (1986). Furthermore, the increase in Bobbie's inner-core rain rates appeared to be caused either by the inward propagation of these CRBs and/or by gradient wind adjustment processes associated with the increase of upper-tropospheric horizontal eddy relative angular momentum flux convergence (ERFC). The ERFC is a measure of a tropical cyclone's asymmetric outflow (i.e., outflow channels) caused by the alignment of the tropical cyclone's outflow with midlatitude or tropical upper-tropospheric troughs (Sadler 1976, 1978). The gradient wind adjustment processes associated with the thermally direct circulation at the entrance region of outflow channels has been proposed by several studies (Challa and Pfeffer 1980; Merrill 1988; Chen and Gray 1985; Molinari and Vollaro 1989; Shi et al. 1990; Rodgers et al. 1991; DeMaria et al. 1993) as a mechanism that enhances the system's inner-core precipitation and intensity.

Although there were sufficient SSM/I observations to resolve Typhoon Bobbie's large-scale CRB cycles during the mature and decaying stages in the case study by Rodgers and Pierce (1995), the SSM/I observations were not frequent enough to resolve the CRB cycles during Bobbie's intensification stage. Furthermore, it was found that the Goddard Scattering Algorithm version 2 developed by Adler et al. (1991) to estimate the spatial distribution of rain rate and total (i.e., combined convective and stratiform) latent heat release (LHR) from SSM/I brightness temperatures in the Bobbie case study could not provide detailed information concerning either the tropical cyclone's vertical distribution of LHR or the fractional contribution by convective precipitation to latent heating.

In the current study, the evolution of Hurricane Opal (1995) is examined, using not only abundant SSM/I observations but also a more sophisticated SSM/I algorithm, which will be employed to estimate the hurricane's total and vertical distribution of LHR and the fractional contribution to LHR by convective precipitation. This algorithm will provide additional information concerning the location and height of the maximum latent heating, and will therefore yield further insight into the tropical cyclone intensification process. In contrast to the Typhoon Bobbie case study, the Hurricane Opal case study will include not only an examination of the mature and rapid decaying stages but also an inspection of the rapidly intensifying stage, which was not forecast well in real time. Most importantly, this study perhaps is unique in utilizing satellite-derived vertical profiles of latent heating distribution in inferring the dynamics of convective bursts and their role in intensification.

Section 2, which follows, includes descriptions of the *F-10*, *F-11*, and *F-13* DMSP SSM/I observations and the algorithms that are used to derive total LHR, latent heating profiles, convective and stratiform rainfall contributions, and total precipitable water (TPW). Section 3 provides an outline of the environmental parameters calculated from ECMWF analyses. A brief background description of Hurricane Opal can be found in section 4. Section 5 details the evolution of Opal's lateral and vertical distribution of latent heating and its relationship to subsequent intensity, including the relationship between the enhanced eyewall total LHR and Opal's rapid intensification. Section 6 identifies sea surface and environmental conditions favorable for the occurrence of an eyewall convective burst. Finally, a summary and discussion of the Opal case study will be presented in section 7.

2. SSM/I-derived parameters

a. The F-10, F-11, and F-13 DMSP SSM/Is

The SSM/Is on board DMSP *F-10*, *F-11*, and *F-13* satellites that were launched in November 1991, November 1992, and May 1995, respectively, measure scattered and emitted microwave radiation at frequencies of 19.35, 22.35, 37.0, and 85.5 GHz. All channels except the 22.35-GHz channel are dual polarized. The SSM/Is complete 14.1 revolutions per day along a near-sun-synchronous orbit at an altitude of 833 km. The approximate times that the ascending branches of the DMSP *F-10*, *F-11*, and *F-13* orbits pass over the central Gulf of Mexico (i.e., 25°N, 90°W) where Opal occurred are, respectively, 1600, 1300, and 1200 UTC. The approximate times of the descending branches of the DMSP orbits over Opal are 12 h later. The SSM/Is scan conically at a constant 45° angle from nadir and have an observational swath width of nearly 1400 km at the earth's surface. Further information concerning the SSM/I sensor and measurements may be found in Hollinger (1991).

b. SSM/I-estimated rainfall rates, convective rain fractions, and latent heating profiles

In this study, the surface rainfall rate R, convective rain fraction f_c, and latent heating rate profile LHR(z) are retrieved using the estimated expected value, or ''Bayesian'' method described by Kummerow et al. (1996) and Olson et al. (1996). All three parameters are retrieved at a horizontal resolution of 12.5 km × 12.5 km. The surface rain rate is defined as the average rain rate over the 12.5 km × 12.5 km area centered on the SSM/I observation. Convective rain fraction is the fraction of the surface rain rate associated with significant ($|w| > 1$ m s^{-1}) cloud updrafts and downdrafts. The latent heating rate at a given level z is the net energy release per unit volume of air due to hydrometeor phase changes (condensation/evaporation, deposition/sublimation, and freezing/melting), averaged over the same 12.5 km × 12.5 km area. Descriptions of the retrieval method and supporting numerical atmospheric model simulations are found in the appendix.

c. Convective and stratiform precipitation contributions to LHR

On the time and space scales of interest in this study, the net latent heating in an atmospheric column is approximately balanced by the equivalent energy flux of surface precipitation, $L_v R$, where L_v is the latent heat of condensation and R is the precipitation rate (see Tao et al. 1993a). The retrieved total latent heat release LHR(z) may therefore be partitioned into convective and stratiform components using the retrieved convective rain fraction f_c:

$$\mathrm{LHR}_c(z) \equiv f_c\ \mathrm{LHR}(z) \tag{1}$$

$$\mathrm{LHR}_s(z) \equiv (1 - f_c)\ \mathrm{LHR}(z), \tag{2}$$

where subscript c denotes convective and s stands for stratiform.

Individual, retrieved latent heating profiles have been aggregated for various analyses in this study. Profiles of LHR, LHR_c, and LHR_s are volume-integrated over the eyewall region (defined here as the region within 55 km of Opal's center) for the purpose of time series plots. Also, profiles of LHR are horizontally averaged over the eyewall region to create composite profiles. In addition, LHR profiles are vertically integrated and then area averaged in 0.5° wide annuli out to 444-km radius from Opal's center to generate time–radius latent heating diagrams.

d. Total precipitable water (TPW)

The SSM/I-estimated *TPW* over ocean regions is derived from an algorithm developed by Petty and Katsaros (1990). The algorithm uses a logarithmic equation to relate the rawindsonde-observed *TPW* to the SSM/Is dual-polarized 19.35-GHz and vertically polarized 22.35-GHz channel by employing a multivariate regression technique. The SSM/I algorithm cannot retrieve *TPW* over land and in raining areas.

3. Environmental influences

To determine whether the SSTs were warm enough (SSTs >26°C) to allow for sufficient moist static energy flux to support convection and to estimate Opal's maximum intensity potential, mean daily SSTs within the regions that Opal traversed are examined. Daily mean SSTs on a 2.0° latitude × 2.5° longitude grid are obtained from the National Meteorological Center (now known as the National Centers for Environmental Prediction) archives.

Tropopause temperatures and 500-mb geopotential heights are also examined to estimate, respectively, Opal's maximum intensity potential and midtropospheric circulation. The tropopause temperatures and the 500-mb geopotential heights are obtained from the European Centre for Medium-Range Weather Forecasts (ECMWF) (Shaw et al. 1987) analyses. The ECMWF analyses are archived on a 2.5° latitude × 2.5° longitude grid, and the environmental parameters are calculated every 12 h (i.e., at 0000 and 1200 UTC). ECMWF grid analyses at finer time and space resolution were not readily available for this study. The ECMWF operational global model analyses are chosen for their ability to accurately analyze tropical systems over data-void ocean regions (Reed et al. 1988). All diagnostic parameters are obtained from the ECMWF data using the GEMPAK 5.1 (des Jardins et al. 1991) grid diagnostic program.

External environmental forcing mechanisms are also examined for their role in initiating, maintaining, and inhibiting Opal's total LHR cycle. The forcing mechanisms analyzed in this study are the vertical wind shear, lower-tropospheric horizontal moisture flux, and upper-tropospheric gradient wind adjustment processes associated with the ERFC within Opal's outflow region. These external forcing parameters are similar to those used in NOAA's Statistical Hurricane Intensity Prediction Scheme (SHIPS) (DeMaria and Kaplan 1994), except for the horizontal tropospheric moisture flux. The forcing parameters are also obtained from the ECMWF analyses.

a. Vertical wind shear

Strong vertical wind shear (m s^{-1}), which is known for its ability to hinder convective growth (Gray 1979; Reuter and Yau 1986; Mundell 1991), is derived from the 850- and 200-mb ECMWF wind analyses. Horizontal winds at the 850- and 200-mb levels are averaged over a 500-km^2 domain centered on the tropical cyclone. The large domain is used to assure more accurate vertical wind shear analyses over the relatively data-void Gulf of Mexico region. The vertical wind shear is estimated by taking the magnitude of the difference between the mean wind vectors at the 850- and 200-mb levels.

b. Upper-tropospheric horizontal eddy relative angular momentum flux convergence (ERFC)

Opal's upper-tropospheric horizontal ERFC (m s^{-1} day^{-1}) is estimated in order to examine the influence of the gradient wind adjustment process associated with Opal's outflow jet on the system's eyewall LHR. To calculate the upper-tropospheric horizontal ERFC, the ECMWF gridded 200-mb Cartesian wind components are first interpolated to 10° azimuthal positions along two concentric circles with radii of 600 and 1000 km centered on Opal's center of circulation. The interpolated Cartesian wind components are then transposed to quasi-Langrangian cylindrical coordinates before ERFC is calculated from (Molinari and Vollaro 1989; DeMaria et al. 1993):

$$\mathrm{ERFC} = -r^{-2}\frac{\partial}{\partial r}(r^2\overline{v_r' v_\theta'}), \tag{3}$$

where r is the radius from the tropical cyclone center, v_r is the radial wind, and v_θ is the tangential wind. The overbar represents an azimuthal average and the prime denotes the deviation from the azimuthal average (i.e., the eddy term). The radial and tangential winds in quasi-Langrangian coordinates are obtained from the ECMWF 200-mb wind analyses. The upper-tropospheric ERFC is calculated for an annulus with inner and outer radii of 600 and 1000 km, respectively, relative to the tropical cyclone's center. Since the satellite-derived upper-tropospheric wind observations used in these analyses may be more abundant outside the data-void central dense overcast (CDO) region, the ERFC analyses are only constructed for annuli outside Opal's CDO region.

c. Mean tropospheric horizontal moisture flux (HMF)

Two of the physical processes that have been shown to influence tropical cyclone LHR within regions of weak lower-tropospheric inertial stability are surface evaporation (Frank 1977) and strong horizontal surges of low-level horizontal water vapor flux (Ooyama 1964; Charney and Eliassen 1964; Molinari and Skubis 1985; Lee 1986). In this study, the mean tropospheric horizontal moisture flux (HMF) is examined in order to ascertain what effect the inward fluxes of water vapor have on precipitation within Opal's inner-core and outer-core region CRBs.

To calculate the mean tropospheric horizontal HMF (10^8 kg s^{-1}), the ECMWF gridded Cartesian wind components and the mixing ratio at the mandatory levels are first interpolated to 10° azimuthal positions along a 333-km-radius circle centered on Opal. The interpolated Cartesian wind components are then transposed to quasi-Lagrangian cylindrical coordinates before HMF is calculated using (Frank 1977)

$$\text{HMF} = \frac{2\pi r}{g} \int_p \overline{v_r q}\, dp, \tag{4}$$

where r is the radial displacement from the tropical cyclone center, q is the mixing ratio, v_r is the radial wind velocity, g is gravity, dp is a vertical pressure increment, and p is the pressure level of integration. The over-bar represents an azimuthal average. The radial winds and mixing ratio are obtained from the ECMWF analyses at mandatory levels up to 300 mb. The mean tropospheric horizontal moisture flux across a cylindrical surface with a radius of 333 km from the center of circulation is calculated between levels of 1000 and 300 mb. The cylinder radius of 333 km is chosen for the following reasons: 1) the radius is greater than the resolution of the ECMWF gridded data (i.e., 2.5° latitude); 2) the cloud track winds that define the environmental lower-tropospheric wind field may be more abundant outside the tropical cyclone's CDO; and 3) earlier water vapor budget studies have indicated that water vapor flux contributes more than surface evaporation to the total precipitation within 333 km of the storm center (Frank 1977). Due to the lack of accurate measurements of surface evaporation and the fact that not all water vapor convergence contributes to precipitation, no attempt is made to relate the changes in the water vapor budget to changes in the eyewall LHR. The evolution of the azimuthal distribution of the water vapor flux at 850 mb (the level of maximum water vapor fluxes) is also calculated from the ECMWF analyses in order to determine the time variation of lower-tropospheric asymmetries of water vapor influx.

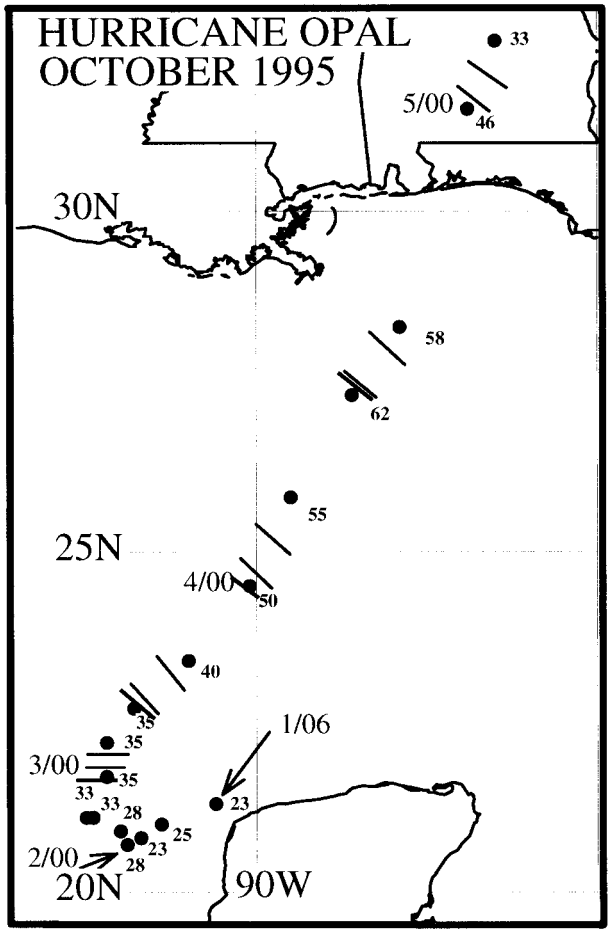

FIG. 1. The 6-h best track positions and intensity (maximum winds in meters per second) for the Gulf of Mexico Hurricane Opal (1–5 October 1995). The lines represent the approximate *F-10, F-11,* and *F-13* SSM/Is observation times.

4. Hurricane Opal

Hurricane Opal was the 15th Atlantic tropical cyclone to occur during the very prolific tropical cyclone season of 1995. Opal formed from an easterly wave that moved westward off the north coast of the Yucatan peninsula into the Gulf of Campeche on 1 October (Fig. 1). It quickly intensified to tropical storm stage as it drifted westward. Slow intensification continued on 2 October,

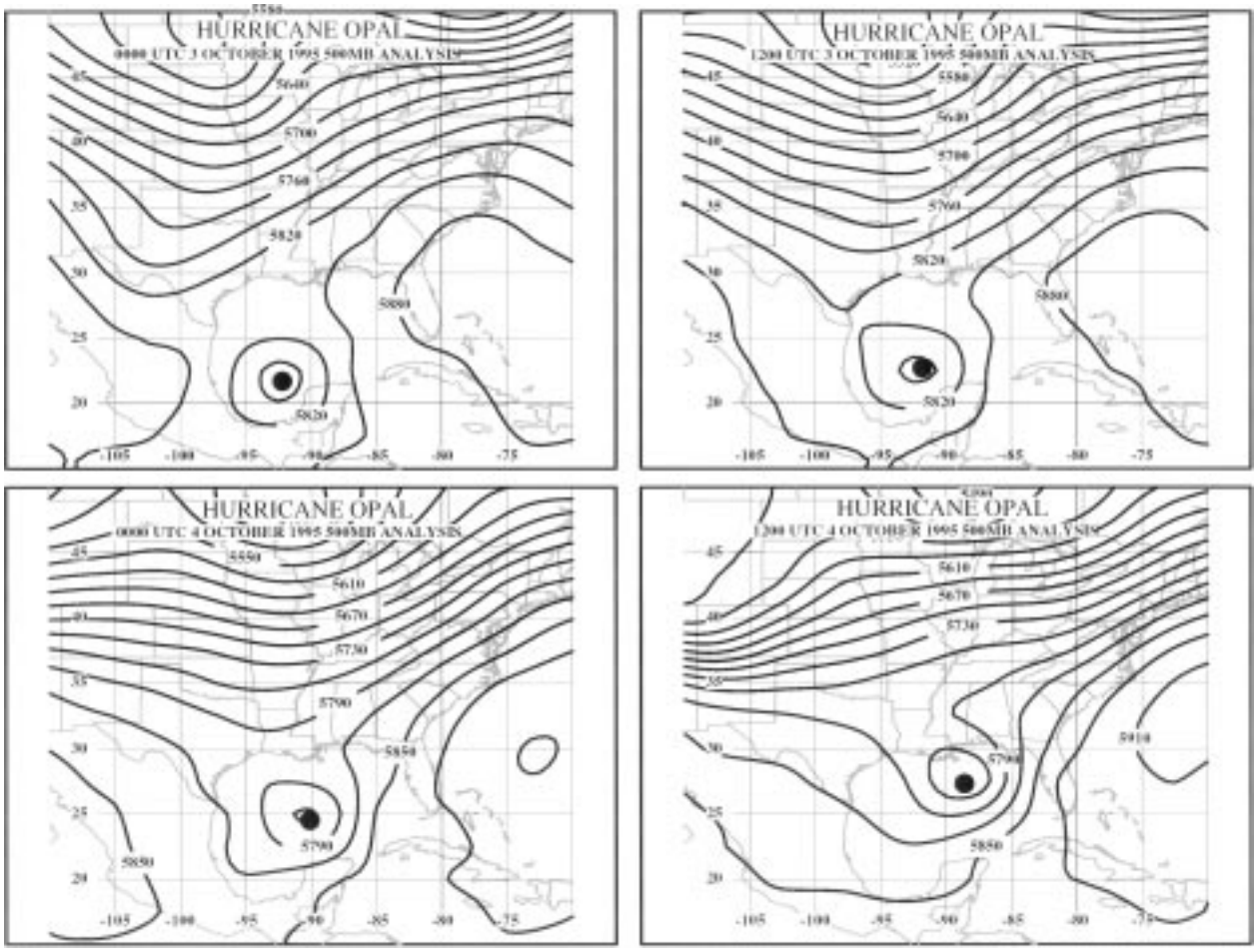

FIG. 2. ECMWF analysis of the North American 500-mb geopotential heights (m) at 0000 and 1200 UTC for 3–4 October 1995. The dot represents Opal's best track position at the given times.

and Opal reached hurricane status at approximately 1200 UTC 2 October.

The ECMWF 500-mb geopotential height analysis seen in Fig. 2 suggests that Hurricane Opal began to interact with a diffluent midtropospheric trough (i.e., a trough that has an upper-level jet located upstream from the base of the trough axis) with an axis that reached the western Gulf of Mexico at 0000 UTC 3 October. In response to this middle-tropospheric trough, Opal recurved northeastward (Fig. 1). Later, Opal merged with the midtropospheric trough circulation as it moved northeastward into the Gulf of Mexico. During this time, Opal accelerated in forward speed and intensified rapidly [as defined by Holliday and Thompson (1979)] from a category 1 to a category 4 hurricane [Saffir–Simpson scale (Simpson 1976)]. This rapid intensification continued for nearly 24 h. Twelve hours prior to landfall, Opal weakened to a category 3 hurricane and made landfall at approximately 2200 UTC 4 October east of Pensacola Beach, Florida, where it caused extensive damage.

5. Opal's latent heating distributions

a. Eyewall total LHR versus intensity

To examine Opal's eyewall total LHR from SSM/I observations, the total LHR is integrated over a cylindrical volume with a radius of 55 km, centered on Opal's best track location, which is interpolated to the SSM/I observation time. Since Opal's eye did not exist or was too small to be resolved at the SSM/I's lower frequencies, no attempt is made to eliminate the eye from the sample. During Opal's early lifetime (1–2 October) there were no SSM/I observations (see Fig. 1). However, Fig. 1 does reveal that from 3 to early on 5 October (2 h after landfall), the *F-10, F-11,* and *F-13* SSM/Is observed Opal's eyewall region 14 times (only a partial SSM/I observation of the eyewall was obtained at 1314 UTC 3 October). For this reason and because of Opal's rapid intensity changes over the Gulf of Mexico, this study will focus on Opal's evolution during 3 and 4 October.

Presented in Fig. 3 are Opal's SSM/I-observed total

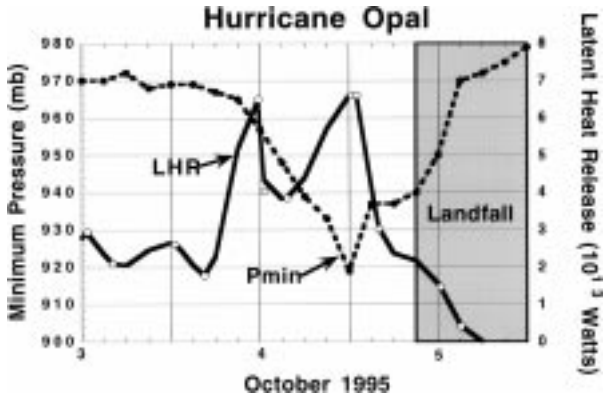

FIG. 3. Opal's minimum central pressure (mb, short dashed lines) and the SSM/I-derived volume-integrated total latent heat release (LHR, 10^{13} W) within Opal's eyewall region (55-km radius from the center)(solid line) for the period of 0000 UTC 3 October to 1200 UTC 5 October. Dots in the LHR curve represent SSM/I observation times. Observational data was interpolated to 3-h time intervals using a spline fit. Stippled region represents the approximate time of Opal's landfall.

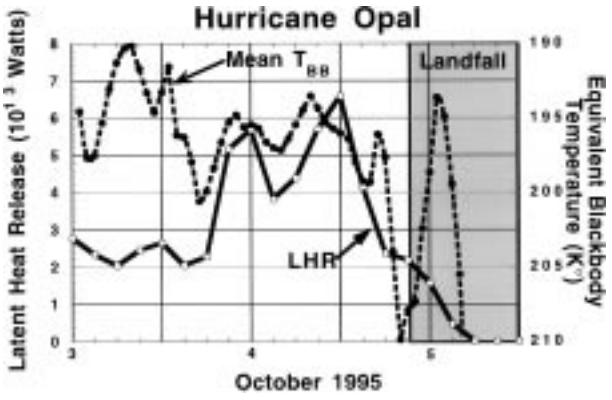

FIG. 4. Opal's 3-h interpolated SSM/I-derived volume-integrated total LHR (10^{13} W) within Opal's eyewall region (solid line) and the 1-h observed GOES-averaged infrared equivalent blackbody temperature (dashed line) for Opal's eyewall region over the period of 0000 UTC 3 October to 1200 UTC 5 October. Stippled region represents the approximate time of Opal's landfall.

LHR in the eyewall region and minimum pressure obtained from the best track (satellite and aircraft fixes). The total LHR is interpolated in time from the SSM/I overpass times to 3-h intervals (using a spline fit) to obtain consistency with the wind maximum observation times. It is obvious that the 3-h minimum central pressure observations are frequent enough to accurately delineate the evolution of Opal's intensity throughout the period. However, it is not clear that the SSM/I observations are frequent enough to accurately describe the evolution of Opal's eyewall total LHR.

To qualitatively verify whether or not the SSM/I observations are capturing the temporal change of total LHR in Opal's eyewall, the hourly GOES mean infrared (window channel) observations are averaged over Opal's eyewall region (the same circular region used in the integration of Opal's SSM/I-derived eyewall total LHR). Assuming that the periods of maximum total LHR and ascending motion in the eyewall region correspond to the periods of minimum mean cloud-top temperatures, it may be possible to verify Opal's SSM/I-derived eyewall total LHR cycle with that derived from GOES observations. From Fig. 4 it may be noted that early on 3 October the low GOES infrared mean equivalent blackbody temperatures (T_{BB}) do not reflect high values of SSM/I-derived LHR. Perhaps the GOES T_{BB}'s are responding to high dense cirrus that is producing relatively light precipitation. However, late on 3 October and during 4 October the GOES-observed T_{BB}'s appear to correspond to the temporal changes in SSM/I-derived total LHR, although the times of maxima (minima) SSM/I-derived total LHR and mean GOES-observed T_{BB}'s are not precisely coincident. When Opal moved over the United States, there was again no correlation between low T_{BB}'s and high values of SSM/I-derived total LHR. Nevertheless, the general correspondence of GOES-observed mean T_{BB}'s and SSM/I-derived total LHR estimates over the majority of the study period suggests that the SSM/I observations were frequent enough to define Opal's large-scale temporal changes in total LHR cycle.

Returning to Fig. 3, the total LHR curve indicates at least two periods when the total LHR reached a maximum in the eyewall region: at approximately 0000 UTC 4 October and 1200 UTC 4 October. The figure also suggests that Opal's minimum pressure decreased after the two episodes of elevated eyewall total LHR (i.e., by as much as 50 mb between 1500 UTC 3 October and 1200 UTC 4 October). It is hypothesized that these episodes of elevated total LHR caused Opal to intensify rapidly during 4 October. It is also inferred from the total LHR and minimum pressure curves that there appears to be greater intensity response with reduced lag time as Opal intensified, albeit the rapid pressure drop between 0900 and 1500 UTC 4 October could possibly be due to nonhydrostatic effects. The increasing response to LHR and subsidence warming of the eye region of Opal as the hurricane intensified may be related to an increase in the lower- and middle-tropospheric inertial stability (Baik 1989). This reduced response time of Opal's minimum pressure to increases in latent heating is consistent with the earlier numerical (Schubert and Hack 1982; Hack and Schubert 1986; Baik et al. 1993; Rodgers et al. 1993, 1994a; van Delden 1989; Shapiro and Willoughby 1982) and observational studies (Rodgers et al. 1994a; Rodgers et al. 1994b; Rodgers and Pierce 1995).

It may also be noted from Fig. 3 that the second episode of elevated eyewall total LHR that peaked at 1200 UTC 4 October had dissipated prior to Opal's landfall. It appears that the dissipation of the second episode of elevated LHR initiated Opal's weakening.

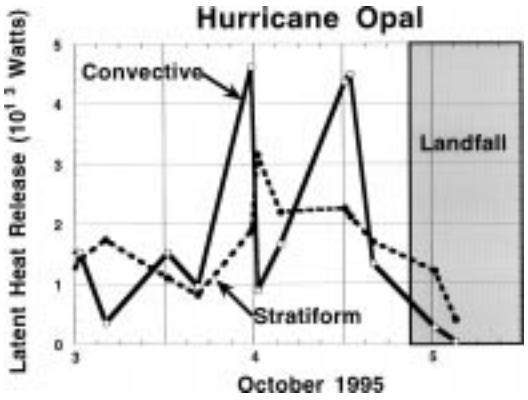

FIG. 5. SSM/I-derived volume-integrated total LHR (10^{13} W) within Opal's eyewall region generated by stratiform (dashed line) and convective (solid line) rain processes for the period of 0000 UTC 3 October to 1200 UTC 5 October. Dots in the LHR curve represents SSM/I observation times. Stipple region represents the approximate time of Opal's landfall.

b. Percentage of convectively generated LHR in Opal's eyewall

The greatest generation of LHR by convective processes in Opal's eyewall region occurred during the periods of elevated total LHR (i.e., 0000 and 1200 UTC 4 October), as illustrated in Fig. 5. The greatest percentage contribution by convective processes was approximately 70%. The SSM/I-derived mean convective percentages in Opal's eyewall are generally consistent with those derived from airborne radar in earlier hurricane case studies (Marks 1985; Marks and Houze 1987). Since the episode of elevated total LHR in the eyewall region consisted of greater convective LHR than during other periods of Opal's life, these episodes of elevated eyewall total LHR will be referred to as a convective burst in the remainder of the text.

c. Vertical distribution of latent heating in Opal's eyewall

The SSM/I-derived vertical distributions of (combined convective and stratiform) latent heating in the eyewall region during the nine SSM/I observation periods are shown in Fig. 6. These latent heating profiles suggest that more net latent heat was generated during the periods of convective burst (i.e., 2345 UTC 3 October and 1216 UTC 4 October), when there was greater generation of latent heating in the mid- and upper troposphere (i.e., above 3 km) by convective processes and relatively little evaporative cooling in the lower troposphere (i.e., below 3 km). These profiles also indicate a greater amount of latent heat generated at upper-tropospheric levels (i.e., above 5 km) during the convective burst episodes (i.e., 2345 UTC 3 October to 1216 UTC 4 October), possibly in response to the enhanced generation of latent heat above the freezing level due to ice microphysical processes. Enhanced LHR above the freezing level, in turn, generates greater eyewall buoyancy. According to Fitzpatrick (1996), eyewall buoyancy must be sufficient to compensate for the loss of eyewall cyclonic momentum due to both frictional dissipation at the surface and export at upper-tropospheric levels. If the ascending motion in the eyewall is strong enough to compensate for the loss of eyewall cyclonic angular momentum, the upward transport of cyclonic momentum will be able to increase the cyclonic tangential wind aloft and, thereby, warm the upper-tropospheric levels due to the thermal wind balance and geostrophic adjustment considerations. Therefore, the greater the eyewall buoyancy and the elevation of latent heating, the more likely latent heating can intensify the system due to higher inertial stability. These satellite observations are consistent with the numerical study by Lord et al. (1984), who showed that ice processes contribute significantly to eyewall buoyancy and hence to tropical cyclone intensification.

Fitzpatrick (1996) also noted that tropical cyclones that had sufficient eyewall buoyancy usually had a vertically stacked vortex in the lower and middle troposphere and an outwardly sloping eyewall in the upper troposphere. In the case of Opal, visible GOES images from 4 October (not shown) suggest that the hurricane was devoid of an eye possibly due to CDO obscuration. Therefore, little information concerning the outward slope of the upper-tropospheric eyewall could be ascertained from the imagery.

A large release of latent heat in the upper troposphere (i.e., above 5 km) does not necessarily indicate a convective burst episode, however. A case in point is the SSM/I-derived latent heating profile (Fig. 6) that was observed at 0409 UTC on 3 October [i.e., the time of cold GOES-observed T_{BB}'s and little SSM/I-derived LHR (Fig. 4)]. The figure clearly shows that the large release of latent heat in the mid- and upper troposphere is compensated by significant evaporative cooling in the lower troposphere (i.e., below 3 km) as stratiform precipitation dominated the total LHR (see Fig. 5). Also, the latent heating profile from the preceding SSM/I overpass at 2357 UTC 2 October exhibits uniform and modest heating up to the 8-km level. Precipitation was generated mainly by stratiform processes during this period (see Fig. 5), likely originating from the dense cirrus CDO, while Opal's intensity was steady state. The sequence from 2357 UTC 2 October to 0409 UTC 3 October may be contrasted to the convective burst period from 2345 UTC 3 October to 1216 UTC 4 October, which was characterized by relatively deep and persistent heating over the entire period. Thus, it may be inferred from Fig. 6 that during convective burst episodes the total eyewall LHR is largely due to large production of midtropospheric latent heating by convective processes and an increasing generation of upper-tropospheric latent heat by ice microphysical processes.

Finally, Fig. 6 suggests that late on 4 October prior to landfall, latent heat production at all levels in the eyewall region decreased. In response to the loss of latent heating, Opal rapidly weakened.

d. Plan views of Opal's total LHR distribution

Presented in Fig. 7 are plan views of Opal's SSM/I-derived, vertically integrated LHR at 0409 and 1630 UTC 3 October and at 0337 and 1558 UTC 4 October. The initial distributions of latent heating (panels a and b) are relatively broad and asymmetric, but by 0337 UTC 4 October (panel c) the storm becomes more compact, with evidence of spiral bands and heating concentrated in the inner core. Later, at 1558 UTC 4 October (panel d), heavy bands of precipitation/latent heating extend further from the storm center and over land.

e. Radial distribution of Opal's total LHR

To examine the temporal change of Opal's horizontal distribution of LHR, vertically integrated LHR is azimuthally averaged over eight annuli, each 55 km in width, extending from Opal's center outward to 444 km. The average LHR values in each annuli are interpolated to 3-h intervals, again using a spline fit, and are presented in time–radius format in Fig. 8. Although the LHR is averaged over large areas, the basic evolution of Opal's large-scale CRBs is resolved. Figure 8, which also shows Opal's minimum pressure at 3-h intervals during 3–5 October, suggests two possible large-scale CRBs (large values of LHR) that are marked by thick dashed lines numbered 1 and 2. The first CRB was initiated approximately 110 km from the center at 1500 UTC 3 October and propagated inward toward the center before dissipating at about 1800 UTC 4 October. This CRB appeared to aid in initiating the first eyewall convective burst at 0000 UTC 4 October.

The second CRB, which first appeared 275 km from the center at approximately 0600 UTC 4 October, propagated inward to within 110 km of the center by 1500 UTC 4 October. The inward propagation of the second CRB appeared to have a significant influence in dissipating the first CRB when it came within approximately 100 km of the first CRB. Early studies by Willoughby et al. (1982) and Willoughby (1988, 1990) have suggested that the subsidence and reduced inward flux of moisture caused by an outer CRB may result in the dissipation of an earlier inward CRB. This interaction most likely caused Opal's second CRB to dissipate the first CRB. The second eyewall convective burst that occurred at 1200 UTC 4 October did not appear to be initiated by the second CRB, but was more likely initiated by external forcing (see section 6c). The second CRB dissipated prior to landfall.

Comparing the region of elevated total LHR associated with the CRB cycle to Opal's minimum pressure, it is evident that the decrease in minimum pressure occurs only when the total LHR is enhanced in the eyewall region of Opal. The magnitude of total LHR in regions outside the eyewall has little influence on Opal's intensity. The figure clearly shows that prior to the development of the first CRB, Opal was in steady state. From the time that the first CRB reached the eyewall region at 2100 UTC 3 October to the time when it dissipated at 1200 UTC 4 October, Opal's minimum central pressure decreased by 50 mb. In the absence of the first CRB after 1200 UTC on 4 October, Opal weakened slowly prior to landfall. These results are consistent with the eyewall total LHR–minimum pressure time series of Fig. 3.

In summary, it appears that Opal's rapid intensification that occurred on 3–4 October was associated with enhanced eyewall total LHR during two episodes of convective burst. During these convective bursts, LHR enhancement may have been caused partly by the inward propagation of the first CRB, where approximately 70% of LHR was produced by convective processes, and the elevated amounts of mid- and upper-tropospheric eyewall LHR, which imply buoyancy and upward vertical motions were large at these levels. These observations support the hypothesis that rapid intensification may occur when the diabatic heating is released close to the center of circulation and as high as possible.

The relationship between Opal's CRB cycles and its intensity is consistent with the mechanisms proposed by Willoughby et al. (1982) and Willoughby (1988, 1990). Similar relationships were deduced from the SSM/I observations of rain rate in four 1989 western North Atlantic hurricanes (Rodgers et al. 1994b) and in the western North Pacific Typhoon Bobbie (Rodgers and Pierce 1995). In the next section, large-scale external forcing mechanisms that may have helped to enhance, maintain, and dissipate the CRBs and eyewall convective bursts are examined.

6. External influences on Opal's LHR

a. Sea surface, surface, and tropopause temperatures

The time evolution of SSTs in the path of Opal and the tropical cyclone's eyewall region total LHR are shown in Fig. 9. It may be noted that Opal encountered a pool of very high SSTs (i.e., greater than 29.5°C) in the middle of the Gulf of Mexico on 3 October. As Opal moved northward toward the coast on 5 October, the tropical cyclone eventually encountered lower SSTs (i.e., approximately 28°C). Throughout Opal's lifetime over the Gulf of Mexico, SSTs were substantially above the critical temperature of 26°C, which is required to support convective growth (Gray 1979).

A time series of tropopause temperatures within Opal's eyewall region during 3–4 October obtained from the ECMWF analyses is presented in Fig. 10. Prior to Opal's landfall at 2100 UTC 4 October, temperatures were less than 193 K, which is nearly 6°C colder than the tropical mean tropopause temperature. Eyewall tropopause temperatures increased by approximately 3°C thereafter.

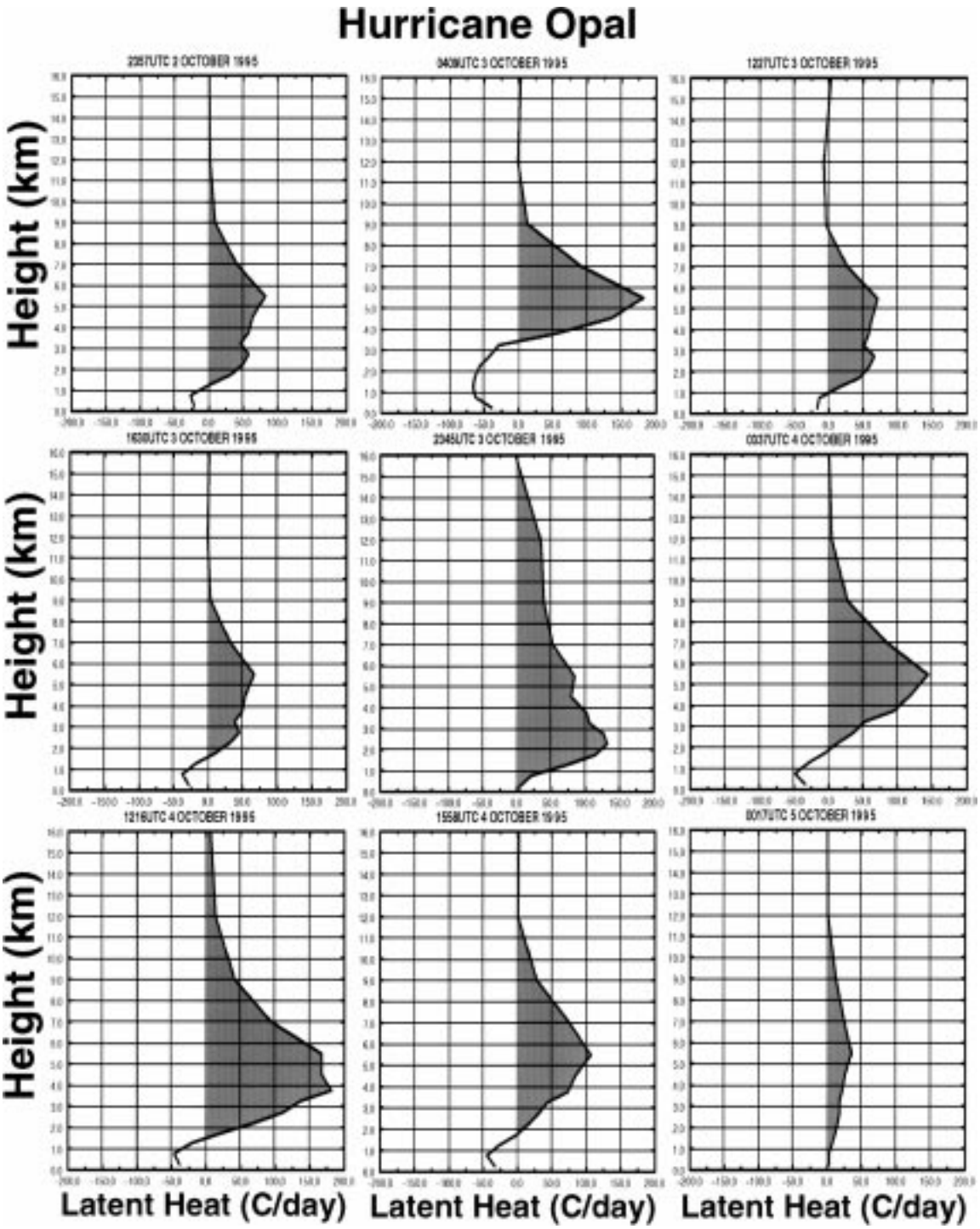

FIG. 6. Vertical distribution (km) of the SSM/I-derived azimuthally averaged LHR (°C day^{-1}) for Opal's eyewall region at nine SSM/I observation times between 3 and 5 October 1995. Positive latent heating rates are shaded.

These low tropopause temperatures (Fig. 10), combined with the high SSTs (Fig. 9), and a humid middle and lower troposphere [derived from the ECMWF analyses (figure not shown)] appeared to have contributed to intensifying Opal to a very intense category 5 hurricane. Utilizing the Carnot cycle theory, which relates SSTs and tropopause temperatures to maximum potential intensity (Emanuel 1991), Opal's potential minimum central pressure is estimated to be less than 820 mb for the given SSTs of 29.5°C and tropopause tem-

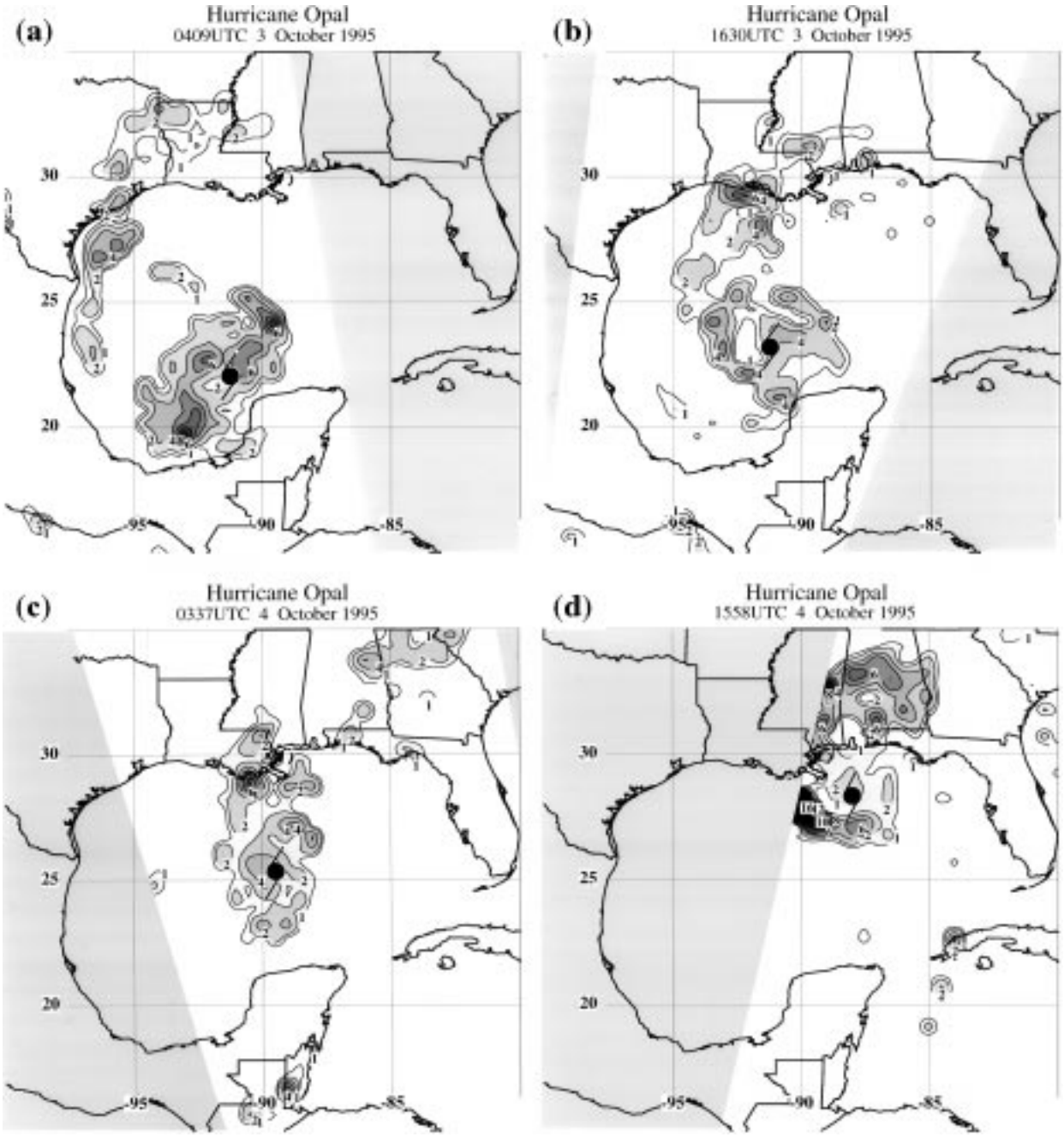

FIG. 7. Plan view of the SSM/I-derived vertically integrated tropospheric LHR (kW m^{-2}) for tropical cyclone Opal at approximately (a) 0409 and (b) 1630 UTC 3 October and at (c) 0337 UTC and (d) 1558 UTC 4 October 1995. The center of Opal is denoted by a hurricane symbol. The white background delineated SSM/I observed rain-free regions and the continuous light gray shade delineates regions not observed by SSM/I. Contour intervals of LHR are 2 kW m^{-2}, and shaded regions delineate LHR greater than 1 kW m^{-2}.

peratures of less than 193 K. On the other hand, Hurricane Florence (i.e., minimum central pressure of 975 mb), which occurred during September 1988 over similar ocean regions with average maximum SSTs of approximately 29.0°C and average tropopause temperatures of 203 K, had a potential minimum central pressure that is 60 mb higher than Opal's. Although the potential minimum central pressure values using Emanuel's (1991) technique are too low due mainly to the overestimation of the relative humidity (Fitzpatrick 1996), the Carnot cycle theory demonstrates the importance of the relationship between sea surface and tropopause temperatures and Opal's potential minimum central pressure.

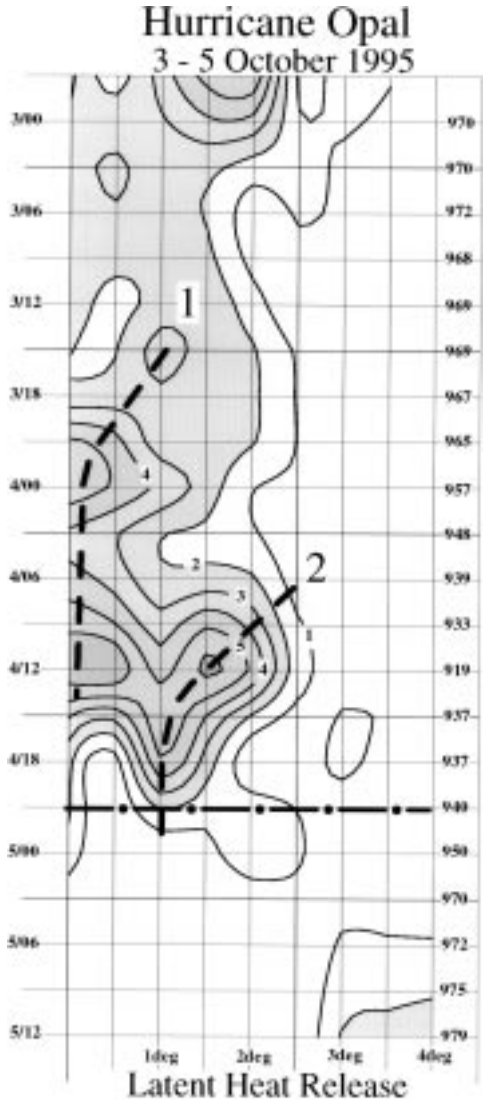

FIG. 8. Time vs radius plot of Opal's 3-h interpolated SSM/I-derived azimuthally averaged [annuli 1 to 8 (55-km width)] total tropospheric LHR (kW m^{-2}) and minimum central pressure (mb) for the period of 2100 UTC 2 October to 1200 UTC 5 October 1995. Contour intervals of LHR are 2 kW m^{-2} and shaded regions delineate LHR greater than 2 kW m^{-2}. The heavy dashed lines (lines 1 and 2) denote the axes of greatest latent heat release. The heavy dashed–dotted line represents the approximate time of Opal's landfall.

b. Upper-tropospheric interaction and vertical wind shear

As mentioned in section 4, Opal interacted with a diffluent 500-mb trough that entered Texas at 0000 UTC 3 October (see Fig. 2). The ECMWF analysis reveals an upper-level jet streak entering the base of the trough at 0000 UTC 4 October, which caused the trough to amplify and merge with Opal. Subsequently, the tropical cyclone intensified as the combined system accelerated northeastward.

The time evolution of the 500 km × 500 km area-averaged vertical wind shear around Opal (Fig. 11) indicates that the vertical wind shear was approximately 15 m s^{-1} prior to 1200 UTC 3 October. However, as Opal moved farther northward into the base of the trough on 4 October, the vertical wind shear surrounding Opal increased to 26 m s^{-1} before Opal made landfall. These vertical wind shear values are substantially larger than the threshold values of 8.5 m s^{-1} needed to inhibit tropical cyclone intensification (Fitzpatrick 1996). The observed vertical wind shear is also substantially larger than the threshold value of 10 m s^{-1} that Rodgers et al. (1994b) and Rodgers and Pierce (1995) found to inhibit the production of rainfall, respectively, in four 1989 North Atlantic hurricanes and in one North Pacific typhoon (i.e., Bobbie). The wind shear in Opal also exceeded the wind shear observed during most of Tropical

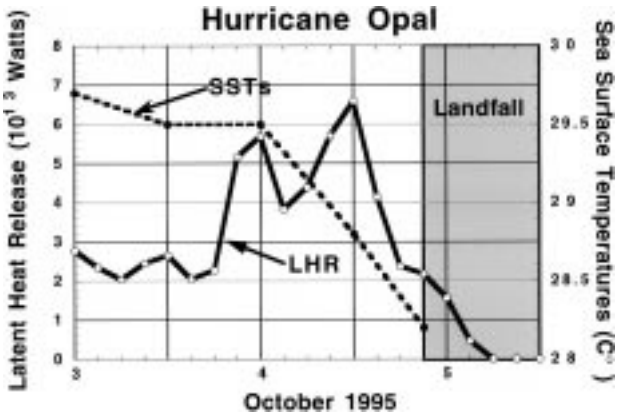

FIG. 9. Opal's 3-h interpolated SSM/I-derived volume-integrated tropospheric LHR (10^{13} W) within Opal's eyewall region (solid line) and the 12-h interval averaged mean sea surface temperatures (°C) (dashed line) that Opal encountered between 0000 UTC 3 October and 1200 UTC 5 October. Stippled region represents the approximate time of Opal's landfall.

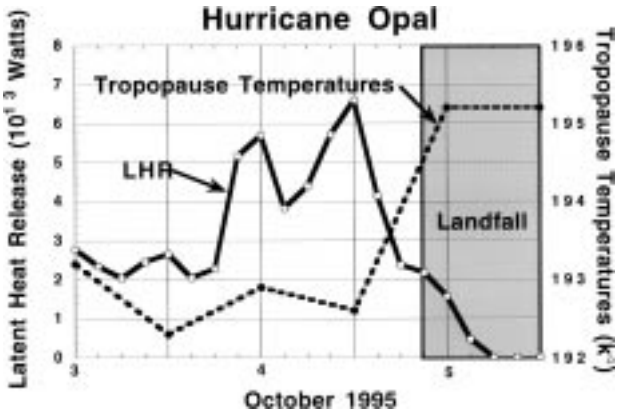

FIG. 10. Opal's 3-h interpolated SSM/I-derived volume-integrated tropospheric LHR (10^{13} W) within Opal's eyewall region (solid line) and the 12-h interval averaged mean tropopause temperatures (K, dashed line) that Opal encountered between 0000 UTC 3 October and 1200 UTC 5 October. Stippled region represents the approximate time of Opal's landfall.

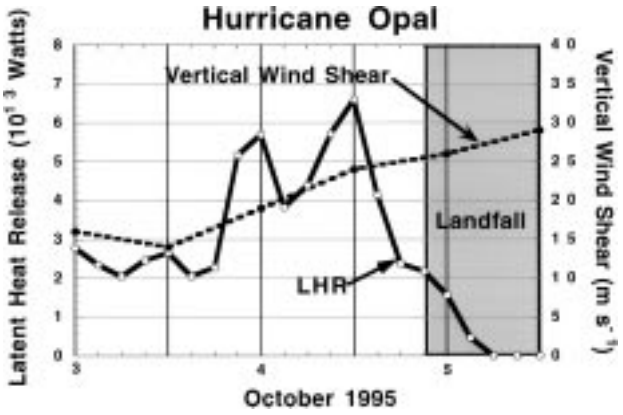

FIG. 11. Opal's 3-h interpolated SSM/I-derived volume-integrated tropospheric LHR (10^{13} W) within Opal's eyewall region (solid line) and the l2-h interval averaged vertical wind shear (m s^{-1}) that Opal encountered (dashed line) between 0000 UTC 3 October and 1200 UTC 5 October. Stippled region represents the approximate time of Opal's landfall.

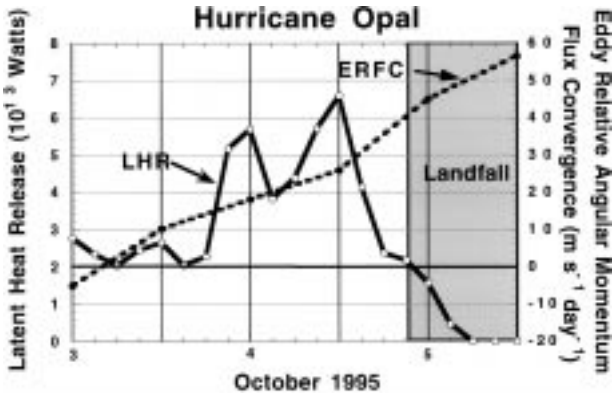

FIG. 12. Opal's 3-h interpolated SSM/I-derived volume-integrated tropospheric LHR (10^{13} W) within Opal's eyewall region (solid line) and the 12-h interval azimuthally averaged upper-tropospheric eddy relative angular momentum flux convergence (ERFC, m s^{-1} day^{-1}) for an annulus bounded by radii of 600 and 1000 km (dashed line) between 0000 UTC 3 October and 1200 UTC 5 October. Positive values are eddy relative angular momentum flux convergence. Stippled region represents the approximate time of Opal's landfall.

Cyclone Florence's (September 1988) lifetime. Nevertheless, the large values of vertical wind shear of up to 25 m s^{-1} before 1200 UTC on 4 October appeared to have had little influence on Opal's convective bursts or CRBs (see Fig. 11).

c. Upper-tropospheric relative angular momentum flux convergence (ERFC)

Figure 12, which depicts the trend of the environmental upper-tropospheric ERFC (within an annulus extending from 600 to 1000 km from Opal's center), suggests that the upper-tropospheric circulation associated with the trough had a negative influence in generating ERFC prior to 0600 UTC 3 October. However, as Opal interacted with the trough, ERFC values increased substantially to nearly 40 m s^{-1} day^{-1} at landfall and to more than 50 m s^{-1} day^{-1} 12 h later. These values of ERFC are considerably larger than those observed in previous developing tropical cyclones (Fitzpatrick 1996). According to DeMaria et al. (1993), an ERFC value of 10 m s^{-1} day^{-1} indicates a period of significant environmental–tropical cyclone interaction and a value of 20 m s^{-1} day^{-1} indicates a period of strong interaction. Initially, the ERFC within the annulus surrounding Opal on 4 October was most likely generated by the formation and enhancement of an outflow channel as Opal first merged with the trough. Later, as Opal moved farther northward and closer to the base of the trough, ERFC seemed to be generated by the trough itself.

When comparing the evolution of Opal's eyewall total LHR with that of the upper-tropospheric ERFC in Fig. 12, it appears that the two episodes of eyewall convective burst (especially the second episode) occurred during the period of increasing ERFC as Opal interacted with the trough [i.e., from 0000 to 1800 UTC 4 October (see Fig. 2)]. A similar relationship was seen in the Tropical Cyclone Florence (September 1988) case (Rodgers et al. 1991; Shi et al. 1990). It may be speculated that the gradient wind adjustment processes associated with the thermally direct circulation in the entrance region of the ascending branch of Opal's outflow channel may have aided in enhancing the eyewall total LHR, particularly during the time when the vertical wind shear was relatively weak. However, since the ECMWF analyses and SSM/I observations are infrequent and do not always coincide, it is impossible to establish a cause and effect relationship between Opal's outflow-induced ERFC and eyewall total LHR. Perhaps finer resolution datasets generated through the use of a mesoscale model may help to resolve the timing of such interactions. As Opal moved farther northward, increasing vertical wind shear associated with the trough appeared to inhibit further convective bursts, even though the ERFC values continued to increase.

d. Tropospheric moisture distribution

1) TOTAL PRECIPITABLE WATER (TPW) DISTRIBUTION

The spatial distribution of the total precipitable water (TPW) observed from SSM/I and derived from the ECMWF analyses (integral of mixing ratio with height) at approximately 0000 and 1200 UTC 4 October 1995 are shown in Figs. 13 and 14, respectively. It is clear from the figures that the SSM/I-observed and the ECMWF-analyzed synoptic-scale TPW fields are generally similar. However, there are subtle small-scale differences caused either by (a) differences in time and resolution of the products, (b) the lack of moisture measurements used in the ECMWF analyses over the Gulf

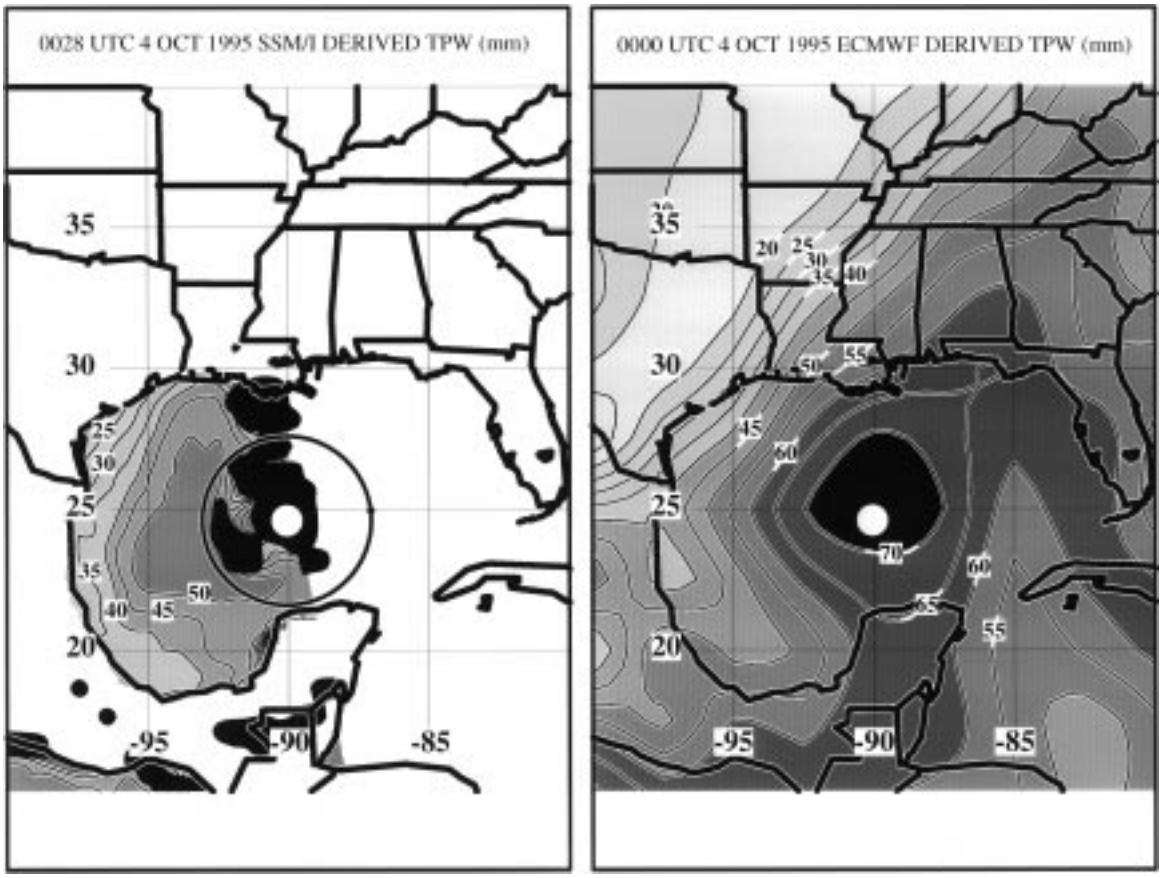

FIG. 13. The SSM/I-observed (left panel) and ECMWF-derived (right panel) environmental total precipitable water (TPW, mm) at approximately 0000 UTC 4 October. Shaded intervals are 5 mm. Black regions in the left panel represent raining areas that the TPW cannot derive from SSM/I. The 222-km-radius circle in the left panel centered on Opal represents the hurricane's approximate circulation circumference. Large white dots indicate Opal's center.

of Mexico, or (c) the inability of the SSM/I to observe TPW over land and in raining areas. Nevertheless, since the ECMWF-analyzed TPW is consistent with the large-scale features observed by the SSM/Is over the Gulf of Mexico, the mean tropospheric and 850-mb HMF derived from the ECMWF analyses are therefore used to determine what influence the distribution of TPW surrounding Opal had in initiating and maintaining the system's CRBs.

Most evident from the ECMWF analyses is the moist troposphere surrounding Opal and a dry region entering the western Gulf of Mexico. The ECMWF analyses of the vertical motion patterns within the trough suggest that the dry region was generated by descending motion west of the trough axis (figure not shown). The ECMWF-derived 850-mb and 500-mb streamline analyses (figures also not shown) suggest that the dry region intruded cyclonically around the western and southern regions of Opal. The more detailed SSM/I figures of TPW indicate an intrusion of dry air from the southwest to within 222 km of Opal's center at approximately 1200 UTC 4 October (see circle in figures). It will be shown that this dry air intrusion helped to terminate the second convective burst (1200 UTC 4 October) through erosion of the LHR in the southern half of Opal prior to landfall.

2) AZIMUTHAL EVOLUTION OF THE 850-MB HORIZONTAL MOISTURE FLUX (HMF)

Figure 15 illustrates the evolution of the azimuthal distribution of the 850-mb HMF at a radius of 333 km from Opal's center from 0000 UTC 2 October to 1200 UTC on 5 October. It is evident that the dry air seen southwest of Opal in Figs. 13 and 14 was entrained into the southwest sector of Opal's outer circulation starting around 1200 UTC on 4 October. It can be inferred from the figure that the southwestern sector of Opal's outer circulation became progressively drier with time as the dry air intruded over the western Gulf of Mexico and interacted with Opal's outer circulation late on 4 October. This dry-air intrusion, combined with the strong vertical wind shear, warmer tropopause temperatures, and cooler SSTs, may have aided in the termination of Opal's second CRB cycle. At the same time, the eastern half of Opal's outer circulation became increasingly moist, which helped to maintain the convective growth

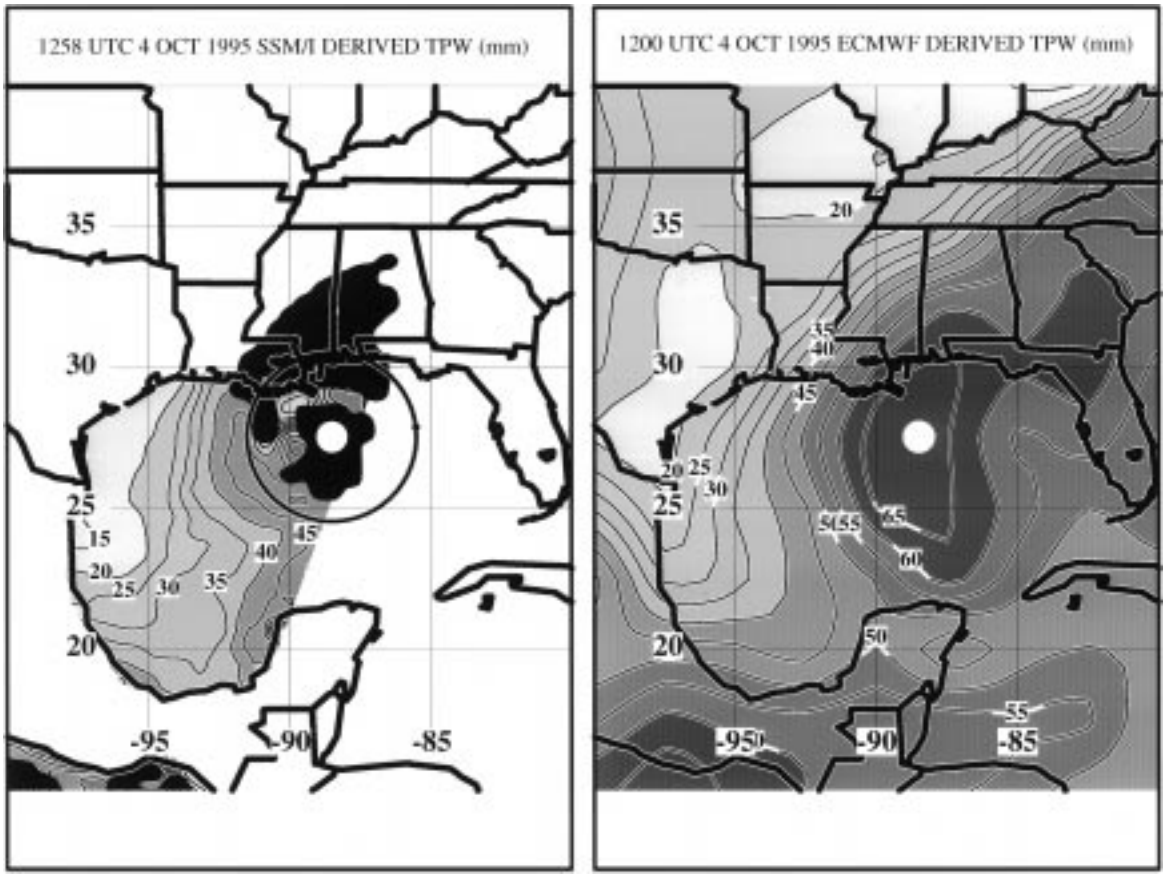

FIG. 14. The same as Fig. 13 but for approximately 1200 UTC 4 October.

in Opal's eastern sector (see Fig. 7). However, as Opal intensified during 4–5 October, the net moisture flux at the 850-mb level continued to increase with time, with maximum values greater than 1100 g kg^{-1} m s^{-1} occurring at 1200 UTC on 5 October. Examination of the 850-mb HMF at the radius of 333 km from Opal's center in a Eulerian frame of reference revealed that the increase in moisture flux values prior to Opal's landfall at 2100 UTC on 4 October were mainly due to the translation of the system and not by net influx of moisture into the system.

3) TROPOSPHERIC MEAN HORIZONTAL MOISTURE FLUX (HMF)

To ascertain what influence the outer-core region tropospheric HMF had in initiating and maintaining Opal's CRBs, the evolution of HMF at a radius of 333 km from Opal's center is compared in Fig. 16 to the evolution of the integrated LHR within an annular volume with inner and outer radii of 165 and 222 km, respectively, centered on Opal (the annular region where Opal's CRBs were first observed by SSM/I). The HMF in the figure undergoes nearly a 23% increase (i.e., 3.1 to 3.8 $\times$ 10^8 kg s^{-1}) in magnitude from 1200 UTC 3 October to 0000 UTC 4 October. These HMF values are nearly a factor of 3 larger than those found at a similar radius surrounding Hurricane Florence. Subsequently, HMF values decreased to a minimum of 2.5 $\times$ 10^8 kg s^{-1} during landfall at 2100 UTC 4 October.

Comparing the HMF values with the volume-integrated LHR during the CRB cycles (Fig. 8), it is clear that the initiation of the CRB cycles occur only when there is a high influx of water vapor and that the high influx of water vapor precedes the initiation of a CRB. However, since the HMF analyses and SSM/I observations are infrequent and do not always coincide, it is not possible to establish a cause and effect relationship between Opal's HMF and the initiation of the CRB cycles. Perhaps, as in the analysis of Opal's upper-tropospheric ERFC, the use of a mesoscale model may help resolve the timing of these interactions.

7. Summary and discussion

The observational study of Tropical Cyclone Opal clearly demonstrates the importance of monitoring the outer-core region CRB cycles and the vertical and spatial distributions of LHR within the tropical cyclone eyewall either by airborne or spaceborne radiometers/

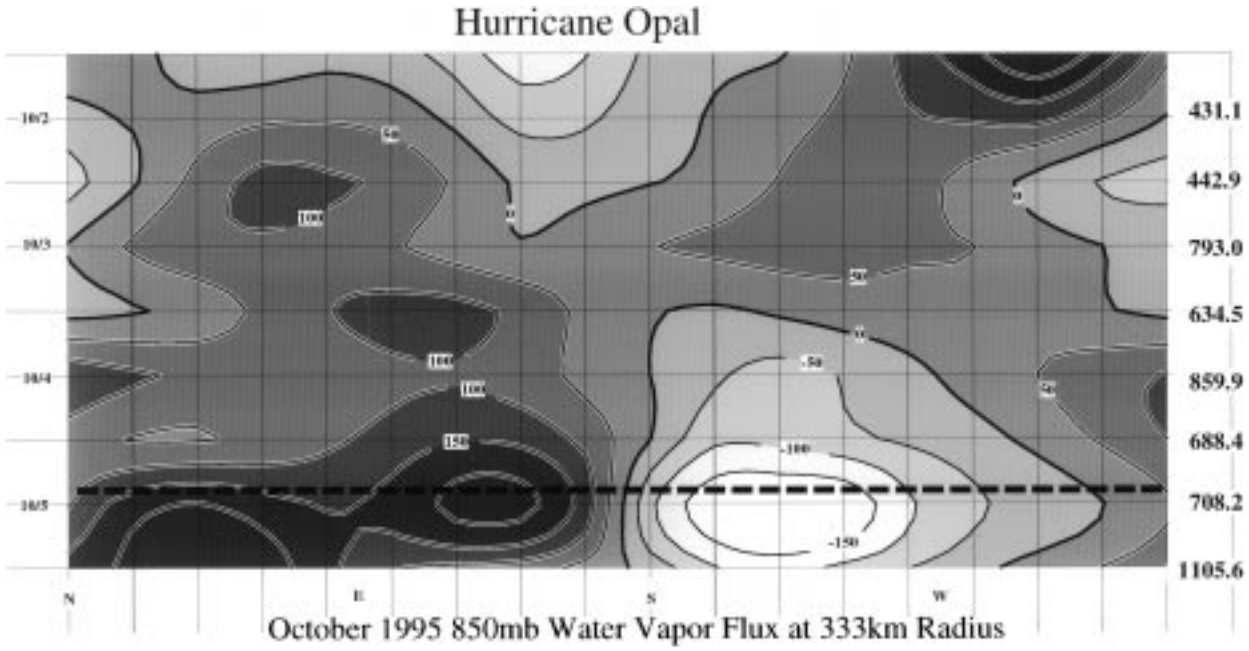

FIG. 15. The azimuthal–time change (1200 UTC 1 October to 1200 UTC 5 October 1995) of Opal's 850-mb horizontal moisture flux (50 g kg^{-1} m s^{-1} contours) across cylindrical surface 333 km from Opal's center. Water vapor flux is calculated in a Lagrangian reference frame. Dark shaded regions denote the inward flux of water vapor. Numbers on the right side of the figure denote net water vapor flux (g kg^{-1} m s^{-1}). Heavy dashed line represents the time of approximate landfall.

radars. SSM/I observations of Opal are shown to be frequent enough to resolve the synoptic-scale evolution of the tropical cyclone's eyewall convective bursts and CRB cycles. The SSM/I observations suggest that the inward propagation of the first CRB appears to aid in initiating and maintaining the first eyewall convective burst at 0000 UTC 4 October. The second CRB, which did not propagate into the eyewall region, appeared to contribute mainly to the dissipation of the first CRB. The second eyewall convective burst that occurred at 1200 UTC 4 October was most likely initiated by external forcing associated with large ERFC values resulting from midtropospheric trough interaction. Also, the observations of Opal suggest that the two eyewall convective bursts were related to the decrease in Opal's minimum pressure and its rapid intensification. It should be noted that there appeared to be little in situ or remotely sensed atmospheric data during this time that could have helped diagnose or forecast a period of rapid intensification.

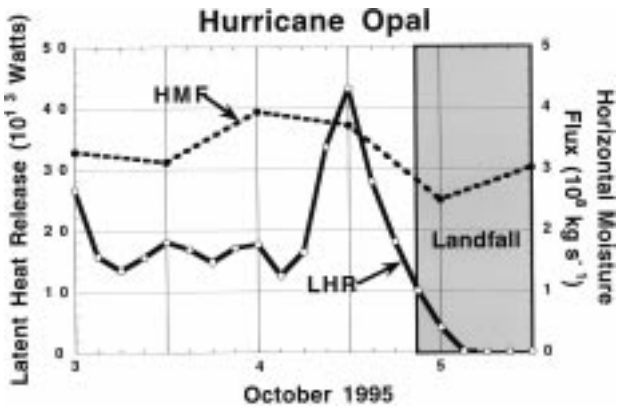

FIG. 16. Opal's 3-h interpolated SSM/I-derived volume-integrated LHR within an annulus of 165–222-km radii from Opal's center (10^{13} W; solid line) and the l2-h interval total (i.e., 1000–300 mb) horizontal moisture flux (HMF, 10^{8} kg s^{-1}) across a cylindrical surface 333 km from Opal's center (dashed line) for the period of 0000 UTC 3 October to 1200 UTC 5 October. Positive values of HMF are moisture inflow. Stippled region represents the approximate time of Opal's landfall.

During Opal's eyewall convective bursts, the SSM/I observations also indicate an increase in the convective contribution to the eyewall-region LHR, particularly at the middle- and upper-tropospheric levels. The increasing middle- and upper-tropospheric eyewall latent heating, most likely from ice microphysical processes, allowed the eyewall to become more buoyant and may have resulted in Opal's rapid intensification (Fitzpatrick 1996). Thus, the SSM/I LHR estimates imply, at least for hurricane Opal, that the release of latent heat at mid- and upper-tropospheric levels close to the tropical cyclone center may lead to a rapid intensification of the system.

Although a direct cause and effect relationship between external forcing and the initiation and maintainence of convective bursts and CRB cycles could not be shown due to the poor spatial and temporal resolution of the ECMWF model-derived diagnostics and SSM/I

observations, atmospheric and sea surface conditions appeared to be more favorable for Hurricane Opal's growth and intensification than those observed in Hurricane Florence (1988) (Rodgers et al. 1991). For example, Opal had a greater intensity potential (i.e., minimum central pressure was approximately 60 mb less) than Florence, since the SSTs and tropopause temperatures were, respectively, approximately 0.5°C higher and 9.0°C lower than the temperatures observed in Florence at times when the storms were located over the Gulf of Mexico. Second, the initial interaction between Opal and the upper-tropospheric trough enhanced ERFC values to a magnitude greater than those observed during Florence's upper-trough interaction. The larger values of Opal's ERFC indicated that gradient wind adjustment processes associated with the entrance region of Opal's outflow may have had a stronger control on the maintanence and enhancement of Opal's eyewall convective bursts, even though Opal's vertical wind shear was significantly greater than that observed in Florence. Finally, Opal's CRBs occurred during a period of elevated outer-region mean tropospheric horizontal moisture convergence, and moisture convergence values were about a factor of 3 greater than those observed with Florence.

The large reduction of total LHR, on the other hand, that occurred after 1200 UTC 4 October and prior to landfall appeared to reflect the dry air intrusion into Opal's outer-core regions. This dry air along with the large increase in vertical wind shear, lower SSTs, warmer tropopause temperatures, and increased subsidence caused by the inward propagation of the outer CRB likely contributed to the termination of Opal's CRBs and may have initiated Opal's final decay prior to landfall.

It is obvious that an evaluation of the spatial and vertical distribution of LHR in a tropical cyclone is important in understanding and predicting its intensity change. This is particularly true if the remotely sensed LHR observations can resolve the CRB and eyewall convective burst cycles. It is also evident that tropospheric and oceanographic conditions have a profound effect on the distribution of LHR and should be monitored to predict changes in tropical cyclone intensity. One way to achieve this is perhaps by directly assimilating remotely sensed observations of LHR into three-dimensional, mesoscale dynamical models as performed recently by Krishnamurti et al. (1993), Karyampudi et al. (1995), and Shi et al. (1996).

Acknowledgments. The authors wish to thank their colleagues Chris Kummerow, Jeff Haferman, Ye Hong, Wei-Kuo Tao, Steve Lang, Yansen Wang, Brad Ferrier, Jeff Halverson, and Dan Johnson for their significant contributions to the latent heating retrieval algorithm development. Studies of convective–stratiform rain classification were enhanced by helpful discussions with Matthias Steiner of Princeton University. Giulia Panegrossi of the Instituto di Fisica dell'Atmosfera/CNR kindly provided the UW-NMS model simulations. The authors would also like to thank Dr. Robert Adler for providing support and valuable comments.

APPENDIX

SSM/I Retrieval of Rainfall Rates, Convective Rain Fractions, and Latent Heating Profiles

a. Retrieval method

The expected value of any retrieved atmospheric parameter x is estimated using

$$\hat{E}[x] = \sum_j x_j \frac{\exp\{-0.5(\mathbf{TB}_O - \mathbf{TB}_s(x_j))^{\mathrm{T}}(\mathbf{O} + \mathbf{S})^{-1}[\mathbf{TB}_O - \mathbf{TB}_s(x_j)] + c(x_j)\}}{\hat{A}}. \quad \text{(A1)}$$

Here, $\mathbf{TB}_O$ and $\mathbf{TB}_s$ are vectors representing observed and computed brightness temperatures, respectively, at the seven SSM/I channel frequencies/polarizations. Here, $\mathbf{O}$ and $\mathbf{S}$ are the error covariance matrices of the observed and computed brightness temperatures, respectively; c is a covective fraction constraint term; and $\hat{A}$ is a normalization factor.

The summation in (A1) is over a large ensemble of cloud/radiative model computations of the atmospheric parameter x and corresponding computed upwelling brightness temperatures, $\mathbf{TB}_s(x)$. These computed atmospheric parameters and brightness temperatures are derived from simulations of tropical/subtropical disturbances performed using three-dimensional, nonhydrostatic numerical atmospheric models. In principle, any atmospheric parameter x simulated by the numerical models can be retrieved using (A1) if there exists sufficient signal in the SSM/I brightness temperature measurements to distinguish different magnitudes of x.

b. Supporting cloud–radiative model simulations

Cloud–radiative model simulations are based upon three-dimensional, nonhydrostatic numerical model simulations from the Goddard Cumulus Ensemble (GCE) model (Tao et al. 1996) and the University of Wisconsin-Nonhydrostatic Modeling System (UW-NMS; Tripoli 1992a). The GCE model was initialized

using NOAA P-3 flight-level data and rawinsonde observations of the environment in immediate advance of a tropical squall line, which occurred 22 February 1993, during the Tropical Ocean Global Atmosphere Coupled Ocean–Atmosphere Response Experiment (TOGA COARE). A 1-km grid-resolution squall-line simulation (TOGA1) on a 128 km × 128 km domain is described in Olson et al. (1996). A subsequent 3-km resolution squall-line simulation on a 384 km × 384 km domain (TOGA3) exhibited storm structure similar to TOGA1, but initiation by a more extensive and cool pool resulted in a much larger storm in the TOGA3 simulation. Observational evidence suggests the existence of a larger cool pool prior to the development of the 22 February squall line (Trier et al. 1996).

Two additional simulations were performed using the University of Wisconsin-Nonhydrostatic Modeling System (Tripoli 1992a). A tropical cyclone simulation (HURRICANE) was initiated using atmospheric observations made at Kingston, Jamaica, 36 h prior to the passage of Hurricane Gilbert (1988). Details of this simulation may be found in Tripoli (1992b). The final 6 h of the HURRICANE simulation utilized a 3.3-km resolution, 205 km × 205 km inner nest, from which atmospheric parameters were extracted for the current analysis. A second UW-NMS simulation of a thunderstorm complex observed during COHMEX was performed on a 1-km resolution, 50 km × 50 km grid. Both the HURRICANE and COHMEX simulations are described in Panegrossi et al. (1998).

Microwave brightness temperatures at the SSM/I frequencies/polarizations are calculated from the high-resolution, model-simulated cloud fields using an Eddington radiative transfer routine. The resulting high-resolution (~1 km) fields of brightness temperatures are then convolved with the SSM/I antenna patterns to simulate antenna diffraction effects. A complete discussion of these brightness temperature calculations may be found in Kummerow et al. (1996). Finally, modeled atmospheric properties spatially coincident with the computed upwelling brightness temperatures are horizontally averaged over 12.5 km × 12.5 km areas. Areas of this size approximate the footprint areas of the highest-resolution, 85.5-GHz SSM/I measurements. Since some of the atmospheric properties of interest are not standard output of the numerical models, a discussion of how these properties are derived from the model simulations follows.

c. Specification of retrieved parameters

Surface rainfall rates are determined from the model simulations in a manner consistent with model physics. Rainfall rates in the GCE model runs are computed from the lowest model level raindrop size distributions. The fallout scheme of Rutledge and Hobbs (1983) is applied to the simulated drop distribution at each model grid point to obtain the surface rainfall rate. Similarly, the fallout calculation described in Flatau et al. (1989) is applied to the raindrop size distributions at the lowest level of the UW-NMS simulations to obtain surface rain rates. Rain rates from either simulation are subsequently area averaged to 12.5 km × 12.5 km resolution and entered, along with other model parameters and simulated brightness temperatures, into the retrieval method's supporting database. Area-average surface rain rate R at 12.5-km resolution may then be retrieved using (A1).

Each horizontal grid point of the high-resolution model simulations is classified as convective or stratiform using the modified Churchill and Houze (1984) technique described in Tao et al. (1993b). The classified model fields are used to determine the convective rain fraction over 12.5 km × 12.5 km areas from

$$f_c \equiv \frac{\sum_i R_i \delta_i}{\sum_i R_i,} \tag{A2}$$

where

$$\delta_i \equiv \begin{cases} 0, & \text{stratiform grid point} \\ 1, & \text{convective grid point.} \end{cases} \tag{A3}$$

Here, R_i is the surface rainfall rate at model grid point i, and the summations are over all grid points within a given 12.5 km × 12.5 km area. Using (A2) and (A3), f_c is calculated for each 12.5 km × 12.5 km area within the numerical model domains and then entered into the retrieval method's supporting database. Therefore, f_c can be retrieved using (A1).

Latent heating profiles are explicitly computed only in the TOGA3 GCE model simulation. In the TOGA 1 GCE and HURRICANE and COHMEX UW-NMS simulations, latent heating profiles at model resolution are estimated from model-simulated thermodynamic and vertical velocity profiles using a simplified form of the first law of thermodynamics:

$$\mathrm{LHR}(z) \cong \rho c_p w \left(\frac{g}{c_p} + \frac{dT}{dz} \right). \tag{A4}$$

Here, ρ is the density of air, c_p is the specific heat of air at constant pressure, w is the vertical velocity, g is the acceleration of gravity, and dT/dz is the rate of change of temperature with height. Mapes and Houze (1995) used scaling arguments to demonstrate that the diabatic contribution to vertical motions dominates the adiabatic contribution in deep, long-lasting heated circulations. Also, since hydrometeor latent heating is a major contributor to the total diabatic heating as shown by Tao et al. (1993b), expression (A4) is generally a reasonable approximation to the latent heating rate. Intercomparisons of explicitly calculated latent heating rates from the TOGA3 simulation and estimated latent heating rates from (A4) are found to be in good agreement.

Once evaluated, the latent heating profiles at model grid resolution are horizontally averaged over 12.5 km $\times$ 12.5 km areas and entered into the retrieval method's supporting database. Latent heating rates within 14 prescribed layers between the surface and 18-km altitude are retrieved using (A1).

REFERENCES

Adler, R. F., H.-Y. M. Yeh, N. Prasad, W.-K. Tao, and J. Simpson, 1991: Microwave simulations of a tropical rainfall system with a three-dimensional cloud model. *J. Appl. Meteor.*, **30,** 924–953.

Baik, J.-J., S.-M. Lee, and C. H. Cho, 1993: Examination of convective process representation and inertial stability in a tropical cyclone model. *J. Korean Meteor. Inc.*, **29,** 308–323.

Challa, M., and R. Pfeffer, 1980: Effects of eddy flux of angular momentum on model hurricane development. *J. Atmos. Sci.*, **37,** 1603–1618.

Charney, J. G., and A. Eliassen, 1964: On the growth of the hurricane depression. *J. Atmos. Sci.*, **21,** 68–75.

Chen, L., and W. M. Gray, 1985: Global view of the upper level outflow patterns associated with tropical cyclone intensity changes during FGGE. Colorado State University Atmospheric Science Paper 392, Fort Collins, CO, 1216 pp.

Churchill, D. D., and R. A. Houze Jr., 1984: Development and structure of winter monsoon cloud clusters on 10 December 1978. *J. Atmos. Sci.*, **41,** 933–960.

DeMaria, M., and J. Kaplan, 1994: A statistical hurricane intensity prediction scheme (SHIPS) for the Atlantic Basin. *Wea. Forecasting*, **9,** 209–220.

——, J.-J. Baik, and J. Kaplan, 1993: Upper level eddy angular momentum fluxes and tropical cyclone intensity change. *J. Atmos Sci.*, **50,** 1183–1147.

des Jardins, M., K. Brill, and S. Schots, 1991: Use of GEMPAK on Unix Workstations. Preprints, *Seventh Int. Conf. on Interactive Information and Processing Systems for Meteorology, Oceanography, and Hydrology*, New Orleans, LA, Amer. Meteor. Soc. 449–451.

Emanuel, K. A., 1991: The theory of hurricanes. *Annu. Rev. Fluid Mech.*, **23,** 179–196.

Fitzpatrick, P. J., 1996: Understanding and forecasting tropical cyclone intensity change. Colorado State University Atmospheric Science Paper 598, Fort Collins, CO, 346 pp.

Flatau, P., G. J. Tripoli, J. Berlinder, and W. Cotton, 1989: The CSU-RAMS cloud microphysics model: General theory and code documentation. Colorado State University Atmospheric Sciences Atmospheric Research Paper 451, Fort Collins, CO, 88 pp.

Frank, W. M., 1977: The structure and energetics of the tropical cyclone. Part 1: Storm structure. *Mon. Wea. Rev.*, **105,** 1119–1135.

Gray, W. M., 1979: Hurricanes: Their formation, structure, and likely role in the tropical circulation. *Meteorology over the Tropical Oceans*, D. B. Shaw, Ed., Roy. Meteor. Soc., 155–218.

Hack, J. J., and W. H. Schubert, 1986: On nonlinear response of atmospheric vorticities to heating by organized cumulus convection. *J. Atmos. Sci.*, **43,** 1559–1573.

Holliday, C. R., and A. H. Thompson, 1979: Climatology characteristics of rapidly intensifying storms. *Mon. Wea. Rev.*, **107,** 1022–1034.

Hollinger, J. O., 1991: DMSP Special Sensor Microwave/Imager calibration/validation. Final Report Vol. 11, 1225 pp. [Available from J. O. Hollinger, Naval Research Laboratory, Washington, DC, 20375.]

Karyampudi, V. M., G. Lai, J. Monobianco, and S. Koch, 1995: Sensitivity of Hurricane Florence (1988) development to initial conditions, assimilation of satellite-derived rainfall rates and convective parameterization schemes. Preprints, *21st Conf. on Hurricanes and Tropical Meteorology*, Miami, FL, Amer. Meteor. Soc., 386–388.

Krishnamurti, T. N., H. S. Bedi, and K. Ingles, 1993: Physical initialization using SSM/I rain rates. *Tellus*, **45A,** 247–269

Kummerow, C., W. S. Olson, and L. Giglo, 1996: A simplified scheme for obtaining precipitation and vertical hydrometeor profiles from passive microwave sensors. *IEEE Trans. Geosci. Remote Sens.*, **34,** 1213–1232.

Lee, C. S., 1986: An observational study of tropical cloud cluster evolution and cyclogenesis in the western North Pacific. Colorado State University Atmospheric Science Paper 403, Fort Collins, CO, 250 pp.

Lord, S. J., H. E. Willoughby, and J. M. Piotrowicz, 1984: Role of a parameterized ice-phase microphysics in an axisymmetric nonhydrostatic tropical cyclone model. *J. Atmos. Sci.*, **41,** 2836–2848.

Mapes, B., and R. A. Houze Jr., 1995: Diabatic divergence profiles in western Pacific mesoscale convective systems. *J. Atmos. Sci.*, **52,** 1807–1828.

Marks, F. D., 1985: Evolution of the structure of precipitation in Hurricane Allen (1980). *Mon. Wea. Rev.*, **113,** 909–930.

——, and R. A. Houze Jr., 1987: Inner-core structure of Hurricane Alicia from airborne doppler radar observations. *J. Atmos Sci.*, **44,** 1296–1317.

Merrill, R. T., 1988: Environmental influence on hurricane intensification. *J. Atmos. Sci.*, **45,** 1678–1687.

Molinari, J., and S. Skubis, 1985: Evolution of the surface wind field in an intensifying tropical cyclone. *J Atmos. Sci.*, **42,** 2865–2879.

——, and D. Vollaro, 1989: External influences on hurricane intensity. Part 1: Outflow layer eddy momentum fluxes. *J. Atmos. Sci.*, **46,** 1093–1105.

Mundell, D. B, 1991: Tropical cyclone intensification. Preprints, *19th Conf. on Hurricanes and Tropical Meteorology*, Miami, FL, Amer. Meteor. Soc., 511–515.

Olson, W. S., C. D. Kummerow, G. M. Heymsfield, and L. Giglio, 1996: A method for combined passive–active microwave retrievals of cloud and precipitation profiles. *J. Appl. Meteor.*, **35,** 1763–1789.

Ooyama, K. V., 1964: A dynamical model for the study of tropical cyclone development. *Geifus Int.*, **4,** 187–198.

Panegrossi, G., S. Dietrich, F. S. Marzano, A. Mugnai, E. A. Smith, X. Xiang, G. J. Tripoli, P. K. Wang, and J. P. V. Poiares Baptista, 1998: Use of cloud model microphysics for passive microwave-based precipitation retrieval: Significance of consistency between model and measurement manifolds. *J. Atmos. Sci.*, **55,** 1644–1673.

Petty, G. W., and K. B. Katsaros, 1990: New geophysical algorithms for the Special Sensor Microwave Imager. Preprints. *Fitfh Int. Conf. on Satellite Meteorology and Oceanography*, London, United Kingdom, Amer. Meteor. Soc., 247–251.

Reed, R. J., A. Hollingsworth, W. A. Heckle, and F. Dell, 1988: An evaluation of the performance of the ECMWF operational system in analyzing and forecasting easterly wave disturbances over Africa and the tropical Atlantic. *Mon. Wea. Rev.*, **116,** 824–865.

Reuter, G. W., and M. K. Yau, 1986: Numerical modeling of cloud development in a shear environment. *Beitr. Phys. Atmos.*, **66,** 65–80.

Rodgers, E. B., and H. F. Pierce, 1995: Environmental influence on Typhoon Bobbie's precipitation distribution. *J. Appl. Meteor.*, **34,** 2515–2532.

——, S. W. Chang, J. Stout, J. Steranka, and J.-J. Shi, 1991: Satellite observations of variations in tropical cyclone convection caused by upper-tropospheric troughs. *J. Appl. Meteor.*, **30,** 1163–1184.

——, ——, and J.-J. Baik, 1993: A satellite observational and numerical study of inner-core diabatic heating and subsequent intensity change in tropical cyclones. Preprints, *20th Conf. on Hurricanes and Tropical Meteorology*, San Antonio, TX, Amer. Meteor. Soc., 189–192.

——, ——, and H. F. Pierce, 1994a: A satellite observational and

numerical study of the precipitation characteristics in western North Atlantic tropical cyclones. *J. Appl. Meteor.* **33,** 129–139.
——, J.-J. Baik, and H. F. Pierce, 1994b: The environmental influence on tropical cyclone precipitation. *J. Appl. Meteor.*, **33,** 573–593.
Rutledge, S. A., and P. V. Hobbs, 1983: The mesoscale and microscale structure and organization of clouds and precipitation in midlatitude cyclones. Part VIII: A model for the ''seeder-feeder'' process in warm-frontal rainbands. *J. Atmos. Sci.*, **40,** 1185–1206.
Sadler, J. C., 1976: Tropical cyclone initiation by the tropical upper-tropospheric trough. *Mon. Wea. Rev.*, **104,** 1266–1278.
——, 1978: Midseason typhoon development and intensity changes and the tropical upper-tropospheric trough. *Mon. Wea. Rev.*, **106,** 1137–1152.
Schubert, W. H., and J. J. Hack, 1982: Inertial stability and tropical cyclone development. *J. Atmos. Sci.*, **39,** 1687–1697.
Shapiro, W. H., and H. E. Willoughby, 1982: The response of balanced hurricanes to local sources of heat and momentum. *J. Atmos. Sci.*, **39,** 378–394.
Shaw, D. B., P. Lonnberg, A. Hollingsworth, and P. Unden, 1987: Data assimilation: The 1984/1985 revisions of the ECMWF mass and wind analysis. *Quart. J. Roy. Meteor. Soc.*, **113,** 533–566.
Shi, J.-J., S. W. Chang, and S. Raman, 1990: A numerical study of the outflow layer of tropical cyclones. *Mon. Wea. Rev.*, **118,** 2042–2055.
——, ——, and ——, 1996: Impact of assimilation of dropwindsonde data and SSM/I rain rate on numerical prodiction of Hurricane Florence (1988). *Mon. Wea. Rev.*, **124,** 1435–1448.
Simpson, R. H., 1976: The hurricane disaster potential scale. *Weatherwise*, **27,** 169–186.
Tao, W.-K., S. Lang, J. Simpson, and R. Adler, 1993a: Retrieval algorithms for estimating the vertical profiles of latent heat release. Their applications for TRMM. *J. Meteor Soc. Japan*, **71,** 685–700.
——, J. Simpson, C.-H. Sui, B. Ferrier, S. Lang, J. Scala, M.-D. Chou, and K. Pickering, 1993b: Heating, moisture, and water budgets of tropical and midlatitude squall lines: Comparisons and sensitivity to longwave radiation. *J. Atmos. Sci.*, **50,** 673–690.
——, S. Lang, J. Simpson, C.-H. Sui, and B. Ferrier, 1996: Mechanisms of cloud-radiation interaction in the Tropics and midlatitudes. *J. Atmos. Sci.*, **53,** 2624–2651.
Trier, S. B., W. C. Skamarock, M. A. LeMone, and D. B. Parson, 1996: Structure and evolution of the 22 February 1993 TOGA COARE squall line: Numerical simulations. *J. Atmos. Sci.*, **53,** 2861–2886.
Tripoli, G. J., 1992a: A nonhydrostatic model designed to simulate scale interaction. *Mon. Wea. Rev.*, **120,** 1342–1359.
——, 1992b: An explicit three-dimensional nonhydrostatic numerical simulation of a tropical cyclone. *Meteor. Atmos. Phys.*, **49,** 229–254.
van Delden, A., 1989: On the deepening and filling of balanced cyclones by diabatic heating. *Meteor. Atmos. Phys.*, **41,** 127–145.
Weatherford, C., 1987: Typhoon structural evolution. Preprints, *17th Conf. on Hurricanes and Tropical Meteorology*, Miami, FL, Amer. Meteor. Soc., 337–340.
Willoughby, H. E., 1988: The dynamics of the tropical cyclone core. *Aust. Meteor. Mag.*, **36,** 183–191.
——, 1990: Temporal changes of the primary circulation in tropical cyclones. *J. Atmos. Sci.*, **47,** 242–264.
——, J. A. Clos, and M. G. Shoreibah, 1982: Concentric eye-walls, secondary wind maxima, and the evolution of the hurricane vortex. *J. Atmos. Sci.*, **39,** 395–411.